SUPPLEMENTARY INFORMATION

Geological setting

The Yap trench is located along the SE convergent boundary of the Philippine Sea plate in the W-Pacific (Fig. DR2A) and constitutes part of the Izu–Bonin–Mariana–Yap–Palau trench-arc system. The trench is ~700 km long and forms a convex shape towards the SE. It reaches a maximum depth of 8946 m at 10º29.957′ N, 138º40.987′ E (Fujiwara et al., 2000). The outcrops of the serpentinites are located on the inner trench slope of the overriding plate of the Yap Trench (Fig. DR2B). The rock sample was recovered by the Human Occupied Vehicle (HOV) *Jiaolong* during Dive 150 (the 38th China scientific survey cruise in 2017, RV Xiangyanghong 09) at 6413 meters below sea-level.

Sample preparation

The serpentinite was exposed on the seafloor and collected by the robot arm of the Human Occupied Vehicle *Jiaolong*. The sample was refrigerated instantly after being recovered and was then transferred into a -80 □ refrigerator. To limit any laboratory contamination, centimeter-sized samples were extracted from the internal regions of the original serpentinite by sawing with sterile, ultrapure water. Prior to cutting, the saw was treated with 5% sodium hypochlorite and then rinsed with sterile, ultrapure water. A thin section was prepared for optical petrographic observations. A part of the remaining sample was subsequently thinned into a resin-free round chip (diameter, 10 mm; thickness, 3 mm) using a stainless steel polishing disc and concentrated ethanol as well as ultrapure water.

Additionally, a broken rock fragment with an unexposed, fresh surface was prepared. Also, the rock chip was subjected to a three-step polishing procedure (I, II, III; Table DR1), followed by electron microscopic observations (Fig. DR7). As a blank, an organic-free sample was also prepared and treated in the same way as all other samples. Ultrapure water and

ultrasonic bath were used to clean the sample before observations. Focused ion-beam (FIB)-foils were prepared in regions of interest after step II.

Table DR1: Polishing procedure of the round rock chip and blank sample.

Step	Polishing method	Analyses
I	Polished with concentrated ethanol, ultrapure water and aluminum oxide on a clean polishing film	SEM (Pt coating)
II	Polished with concentrated ethanol, ultrapure water and aluminum oxide on a clean polishing film	FIB-SEM (Pt coating) TEM
III	Ar ion-beam polishing	SEM (Pt coating)

SEM and Raman analyses reveal the presence of organic matter in the round chip after each polishing step as well as in the broken rock fragments (Figs. DR 7A, B), whereas no carbon was detected in the polished blank sample. These observations imply that the organic matter was not introduced during the polishing procedure and is part of the original sample collected at the seafloor.

We also prepared a FIB-foil of an area with the serpentinite that does not contain any organics as a reference sample. Energy-dispersive X-ray (EDX)-scanning transmission electron microscopy (STEM) mapping of this reference sample did not detect any carbon. This demonstrates that carbon-contamination due to insufficient decomposition of the Pt-metal-organic precursor (i.e., $C_5H_4CH_3Pt(CH_3)_3$), during FIB-scanning electron microscopy (SEM) sample preparation, does not produce detectable organic signatures in the samples.

Estimation of CO_2 required to generate CCM

Assuming individual CCM has the same distribution and chemical composition, the equation of required CO_2 can be written as follows:

$$\rho = \frac{a\rho_0 M}{M_0}$$

where ρ is the density of CO_2, ρ_0 is the density of CCM (1200 kg/m^3, immature kerogen; Okiongbo et al., 2005), a is the proportion of CCM in serpentinite, M and M_0 are molecular mass of CO_2 (44 g/mol) and CCM (12 g/mol) respectively. The partially altered peridotite has up to ~4 vol.% porosity with 99.7 vol.% pores size < 100 nm (Tutolo et al., 2016). According to TEM observations, ~70 vol.% individual pore is filled with CCM, and 10% of the nanoporosity is assumed to be catalytically active. We therefore estimated that there are 0.28 vol.% CCM in serpentinite, which can eventually sequester 12.3 kg/m^3 (280 mol/ m^3) CO_2.

Methods

All analyses were conducted at Utrecht University, the Netherlands.

Scanning electron microscopy

Overview SEM imaging was carried out on Pt-coated specimens, using a JEOL JCM-6000 in backscattered electron (BSE) mode. Standard operating conditions for SEM imaging was 15 kV accelerating voltage at a working distance of 20 mm.

Focused ion-beam-scanning electron microscopy & transmission electron microscopy

FIB-SEM investigations were carried out on Pt-coated specimens in secondary electron and backscattered electron modes under high vacuum, using a FEI Helios Nanolab G3. Analytical conditions were 2-15 kV accelerating voltage, low current (0.1 nA) and a 4 mm working distance. Energy-dispersive X-ray (EDX) spectroscopy analyses were carried out with an Oxford INCA-350 spectrometer. The FIB-SEM was also used to prepare electron-transparent thin foils (final thickness <100 nm). These foils were subsequently analyzed using a FEI Talos F200X TEM operated at 200 kV. Bright-field (BF), dark-field (DF) and high-angle annular dark-field (HAADF) images were collected simultaneously. High-sensitivity two-dimensional EDX chemical mapping was executed using the FEI Super-EDX setup. Continuous monitoring

of HAADF images generated during EDX-STEM mapping allowed us to minimize the electron beam-induced damage of the carbonaceous matter. All processing and peak deconvolution was done in the Bruker ESPRIT 1.9 software package.

Raman spectroscopy

Raman spectra were obtained with a WiTec alpha 300R Raman microscope using the 532 nm wavelength laser operating at a power less than 1mW, to avoid graphitization of the complex carbonaceous material, with integration times of 10 s. Raman spectra were collected using a 50× objective. Each selected spectrum was fitted using the Fast Fourier transform method after being backgrounds subtracted to a polynomial function. Assignment of molecular vibrations is based on published data (Socrates, 2001; Goto et al., 2016).

Photo-induced force microscopy

Photo-induced force Microscopy (PiFM) experiments were performed using a VistaScope microscope (Molecular Vista, Inc.). AFM micrographs of varying sizes (0.5-50 μm), but set resolution (256 x 256 pixels), were measured in dynamic non-contact mode using NCHAu tips (Nanosensors). Infrared data was collected using a Block Engineering tunable quantum cascade laser (QCL) as mid-IR source providing an IR working range of 775-1970 cm^{-1}.

After acquiring topography information, IR information was collected in three forms: 1) single point IR spectra, 2) IR images at set wavenumbers, and 3) hyperspectral (hyPIR) images with a full IR spectrum measured at each pixel. The single point IR spectra were taken with an acquisition time of 500 ms, a resolution of 4 cm^{-1}, and were averaged (up to 40 times). These near-field infrared measurements were performed with an approximate lateral resolution of 10 nm and a probing depth of 30 nm (Fu et al., 2017). The IR images were taken after identifying relevant IR wavenumbers from the point spectra. They were taken simultaneously with topography images by tuning detection of the topography signal to the second-, and IR signal to the first Eigenmode of the AFM cantilever. HyPIR images were typically taken at lower

resolution (128 x 128 pixels) to decrease measurement time. Spectrum acquisition time varied between 300-600 ms, and the scanning speed was adjusted accordingly.

The PiFM data (AFM micrographs, point spectra, IR images) was processed using SurfaceWorks software (Molecular Vista, Inc.). The hyPIR image datasets were analyzed using Principle Component Analysis (PCA) function provided in the TXM-XANES-Wizard software package (Liu et al., 2012). Prior to PCA analysis, the hyPIR images were normalized by dividing them by their sum image and multiplied in order to have spectral intensities larger than 1 (a.u.). Subsequently, the image stacks were cropped, and the data was mean-centered. A number of Principle Components (typically 3-4) were chosen after inspection of their scree plot and Eigenspectra for k-means clustering. For the clustering, the number of clusters was (at least) twice the number of PCs, and k-means replicates was set to 10. Subsequently, EM for GMM clustering was applied. The resulting clusters and their spectra were inspected for information. Clusters would be merged or removed if they showed superfluous information. The result would be an image with the lowest amount of clusters which could still accurately describe all spectral features.

Differences in Raman and PiFM spectra could be due to either natural variations or differences between bulk vibrational spectroscopy, i.e., Raman spectroscopy, and true surface-mode spectroscopy, i.e., PiFM. Raman spectroscopic analyses of micron-sized CCM across the serpentine fragments.

Supplemental Acknowledgements

We thank Dr. Lingmin Zhang (Tongji University) for assistance with EMP analyses, Tilly Bouten (Utrecht University) for assistance with SEM analyses and Kaibo Nan (Shanghai University) for assistance with porosity distribution calculations.

References of Data Repository

114 Chen, W., Zheng, H., Teng, H., Wang, Y., Zhang, Y., Zhao, C. and Liao, Y., 2015,
115 Enhanced Coagulation-Flocculation Performance of Iron-Based Coagulants:
116 Effects of PO_4^{3-} and SiO_3^{2-} Modifiers: PloS one, v. 10.
117 Doidjo, M.T., Belec, L., Aragon, E., Joliff, Y., Lanarde, L., Meyer, M., Bonnaudet, M. and
118 Perrin, F.X., 2013, Influence of silane-based treatment on adherence and wet
119 durability of fusion bonded epoxy/steel joints: Progress in Organic Coatings, v. 76,
120 p. 1765–1772.
121 Fu, D., Park, K., Delen, G., Attila, Ö., Meirer, F., Nowak, D., Park, S., Schmidt, J.E. and
122 Weckhuysen, B.M., 2017, Nanoscale infrared imaging of zeolites using
123 photo-induced force microscopy: Chemical Communications, v. 53, p. 13012–
124 13014.
125 Fujiwara, T., Tamura, C., Nishizawa, A., Fujioka, K., Kobayashi, K. and Iwabuchi, Y.,
126 2000, Morphology and tectonics of the Yap Trench. Marine Geophysical
127 Researches, v. 21, p. 69–86.
128 Goto, Y., Shimizu, K.I., Kon, K., Toyao, T., Murayama, T. and Ueda, W., 2016,
129 NH_3-efficient ammoxidation of toluene by hydrothermally synthesized layered
130 tungsten-vanadium complex metal oxides: Journal of catalysis, v. 344, p. 346–353.
131 Haberhauer, G. and Gerzabek, M.H., 1999, Drift and transmission FT-IR spectroscopy of
132 forest soils: an approach to determine decomposition processes of forest litter,
133 Vibrational Spectroscopy: v. 19, p. 413–417.
134 Kelemen, P.B., Matter, J., Streit, E.E., Rudge, J.F., Curry, W.B. and Blusztajn, J., 2011,
135 Rates and mechanisms of mineral carbonation in peridotite: natural processes and
136 recipes for enhanced, in situ CO_2 capture and storage: Annual Review of Earth and
137 Planetary Sciences, v. 39, p. 545–576.
138 Lafuente B., Downs R. T., Yang H., Stone N., 2015, The power of databases: the RRUFF

project, in: Highlights in Mineralogical Crystallography, Armbruster T. and Danisi R.M.: Berlin, Germany, W. De Gruyter, p. 1–30.

Li, L., Zhang, X., Luan, Z., Du, Z., Xi, S., Wang, B., Cao, L., Lian, C. and Yan, J., 2018, In situ quantitative Raman detection of dissolved carbon dioxide and sulfate in deep□sea high□temperature hydrothermal vent fluids: Geochemistry, Geophysics, Geosystems, v. 19, p.1809–1823.

Liu, Y., Meirer, F., Williams, P. A., Wang, J., Andrews, J. C., and Pianetta, P., 2012, TXM-Wizard: a program for advanced data collection and evaluation in full-field transmission X-ray microscopy: Journal of synchrotron radiation, v. 19, p. 281–287.

Ménez, B., Pisapia, C., Andreani, M., Jamme, F., Vanbellingen, Q.P., Brunelle, A., Richard, L., Dumas, P. and Réfrégiers, M., 2018, Abiotic synthesis of amino acids in the recesses of the oceanic lithosphere: Nature, v. 564, p. 59–63.

Okiongbo, K.S., Aplin, A.C. and Larter, S.R., 2005, Changes in type II kerogen density as a function of maturity: Evidence from the Kimmeridge Clay Formation: Energy & fuels, v. 19, p. 2495–2499.

Reagan, M. K., et al., 2017, Geodynamic implications of crustal lithologies from the southeast Mariana forearc: Geosphere, v. 14, p. 1–22.

164

Rodriguez, J.A., Llobera, A. and Dominguez, C., 2000, Evolution of the mechanical stress on PECVD silicon oxide films under thermal processing: Journal of materials science letters, v. 19, p. 1399–1401.

Socrates, G., ed., 2001, Infrared and Raman characteristic group frequencies: tables and charts: Chichester, U.K., John Wiley and Sons, 347 p.

Verma, S.P., 1986, Low levels of irradiation modify lipid domains in model membranes: a laser Raman study: Radiation research, v. 107, p. 183–193.

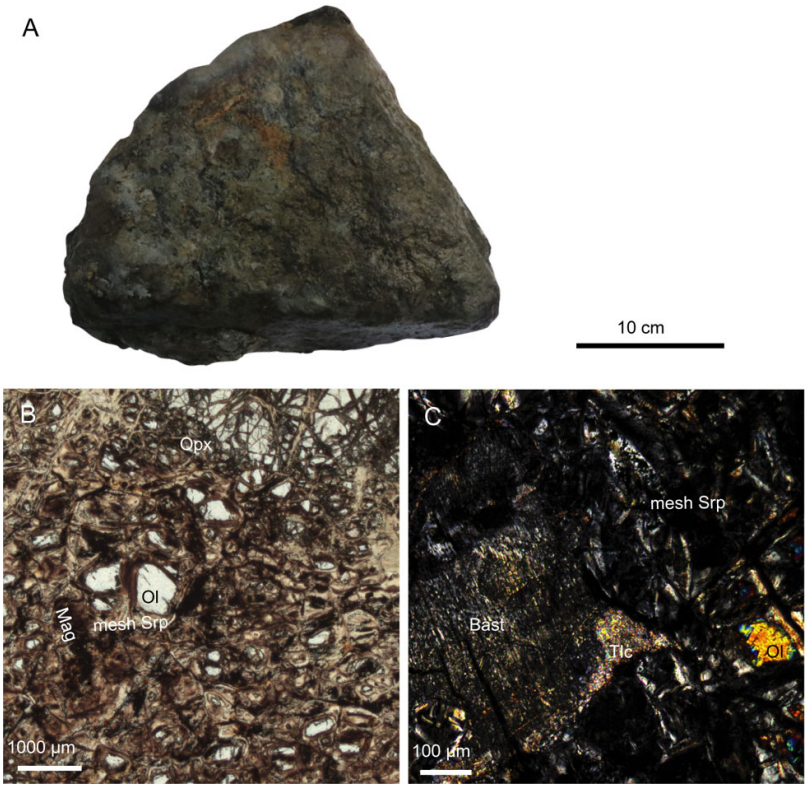

Figure DR1. Optical images of the partly serpentinized harzburgite recovered by the Human Occupied Vehicle *Jiaolong* at the Yap Trench (6413 m below sea level). (**A**) Photograph of the dark-green hand specimen on board. (**B-C**) Cross-polars photomicrographs showing hydrated paragenesis, which is composed of mesh serpentine (mesh Srp) + magnetite

178 (Mag), and bastite (Bast) + talc (Tlc), after olivine (Ol) and orthopyroxene (Opx; < 50 vol.%)
179 respectively.

Table DR2. Electron microprobe analyses (%wt) measured on mesh serpentine and relic olivine. Values are average and 2σ. *n*, number of analyses; b. d. l., below detection limit; $(FeO)_T$, total ferric and ferrous iron; X_{Mg}= MgO/ (MgO + FeO_T).

Mineral:	Olivine	Mesh serpentine
n:	12	13
wt. %		
SiO_2	41.23 (0.39)	40.21 (1.78)
TiO_2	0.01 (0.01)	b. d. l.
Al_2O_3	0.02 (0.01)	0.30 (0.33)
Cr_2O_3	0.02 (0.01)	0.08 (0.07)
$(FeO)_T$	8.27 (0.14)	5.12 (1.29)
MgO	49.86 (0.88)	36.79 (1.85)
MnO	0.11 (0.03)	0.04 (0.04)
CaO	0.06 (0.03)	0.08 (0.04)
K_2O	b. d. l.	0.01 (0.01)
Na_2O	b. d. l.	0.02 (0.02)
Total	99.67 (1.09)	82.76 (1.35)
X_{Mg}	0.86 (0)	0.88 (0.03)

180

181

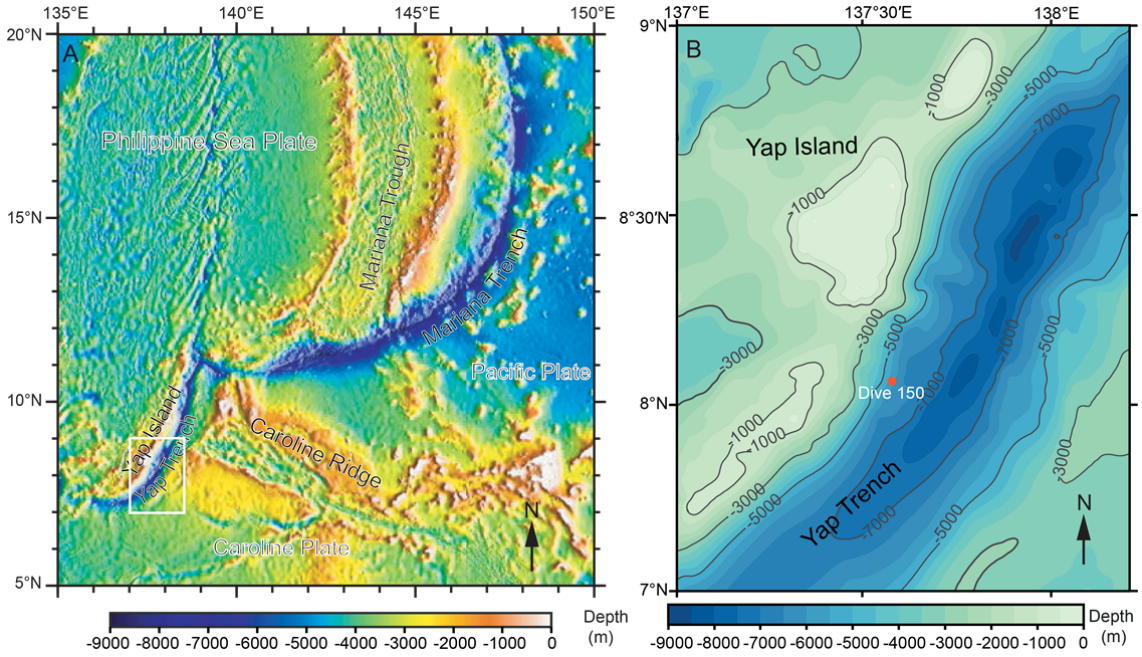

Figure DR2. The Mariana-Yap subduction zone and location of the sampling site. (**A**) Bathymetry map of the Yap and Mariana Trench (modified from Reagan et al., 2017). The maximum water depth of the Yap Trench reaches 8946 m. The white box depicts the studied area as shown in (B). (**B**) Dive 150 and sampling site (8.0514°N, 137.5949°E, 6413m; WGS84) executed by HOV *Jiaolong*.

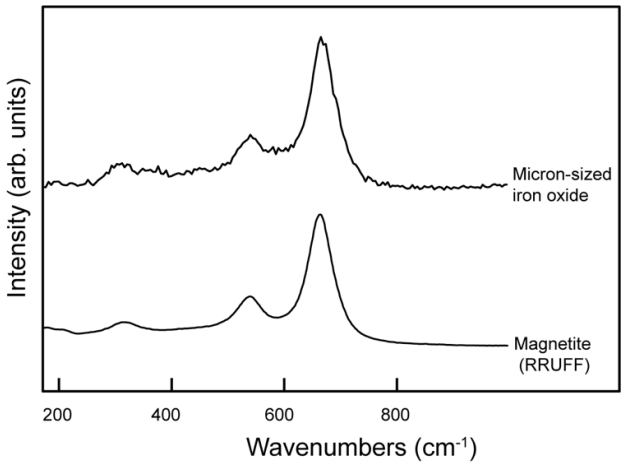

191

192 **Figure DR3.** Raman spectra of the micron-sized iron oxide grains shown in Fig. 1A of the
193 main text are consistent with magnetite according to the RRUFF database (Lafuente et al.,
194 2015).

195

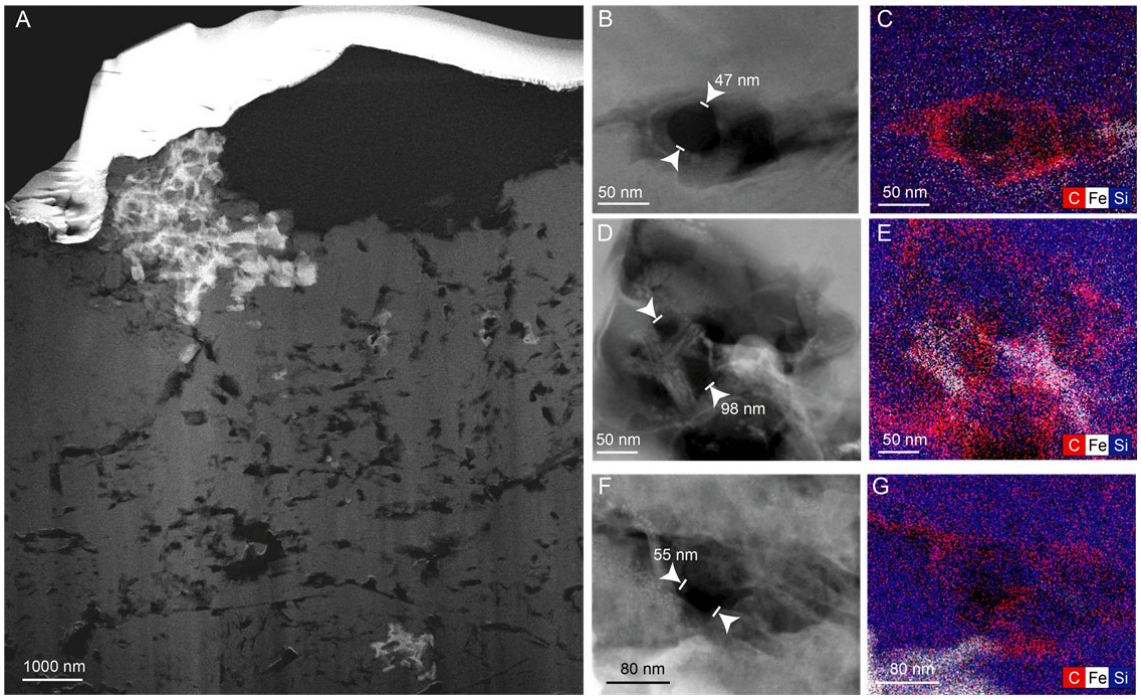

Figure DR4. Nanopores and related COM within mesh serpentine. (A) HAADF-STEM image of the FIB-foil showing nanopores below the micro-sized CCM. (B, D, F) High-resolution HAADF-STEM images of nanopores. (C, E, G) Corresponding elemental distributions for iron (white), carbon (red) and silicon (blue) in A. The association between carbon-rich material in the nanopore and the Fe-(hydr)oxide on the right of the image is clearly visible.

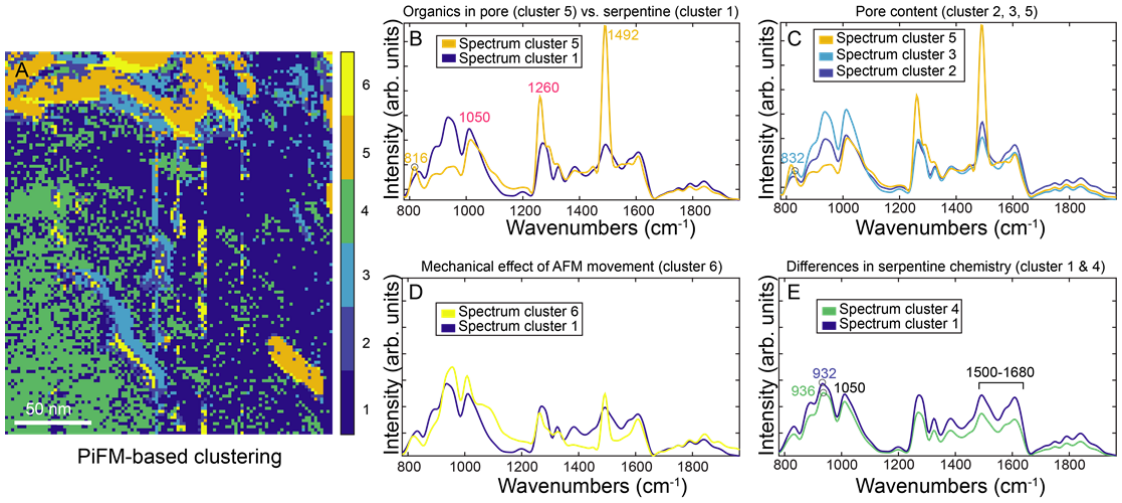

204

205 **Figure DR5. Results of the Principle Component Analysis (PCA, see Methods) of the**
206 **PiFM hyperspectral maps.** (**A**) Cluster map from hyperspectral IR (hyPIR) image shown in
207 Fig. 3 of the main text. (**B-E**) Comparison of the different spectra obtained from the PCA
208 cluster analysis revealing the presence of aromatic compounds (cluster 5) and iron oxide
209 (cluster 2) within serpentine nanopores. Differences in serpentine spectra (cluster 1 and 4) may
210 have been caused by variation of Si-O-H bending modes. Cluster 6 in **(D)** shows the effect of
211 AFM tip noise/dragging on spectrum acquirement.

212

Table. DR3. Assignment for the PiFM bands of nanosized CCM and related minerals within mesh serpentine (Fig. 3 and Fig. DR5). M represents cations in the hydrated silicate structure (e.g. Fe or Mg). Band assignments are based on refs. Ménez et al., 2018; Haberhauer and Gerzabek, 1999; Chen et al., 2015; Doidjo et al., 2013; Rodriguez et al., 2000.

Wavenumber (cm^{-1})	**Assignment**
816	Aromatic C-H out-of-plane bending
832	Fe-O-Fe stretching
932	Si-O-H bending
936	Si-O-H bending
1050	Si-O stretching & AFM tip contamination
1260	AFM tip contamination
1492	Aromatic C=C stretching
1500-1680	M-O-H bending

213

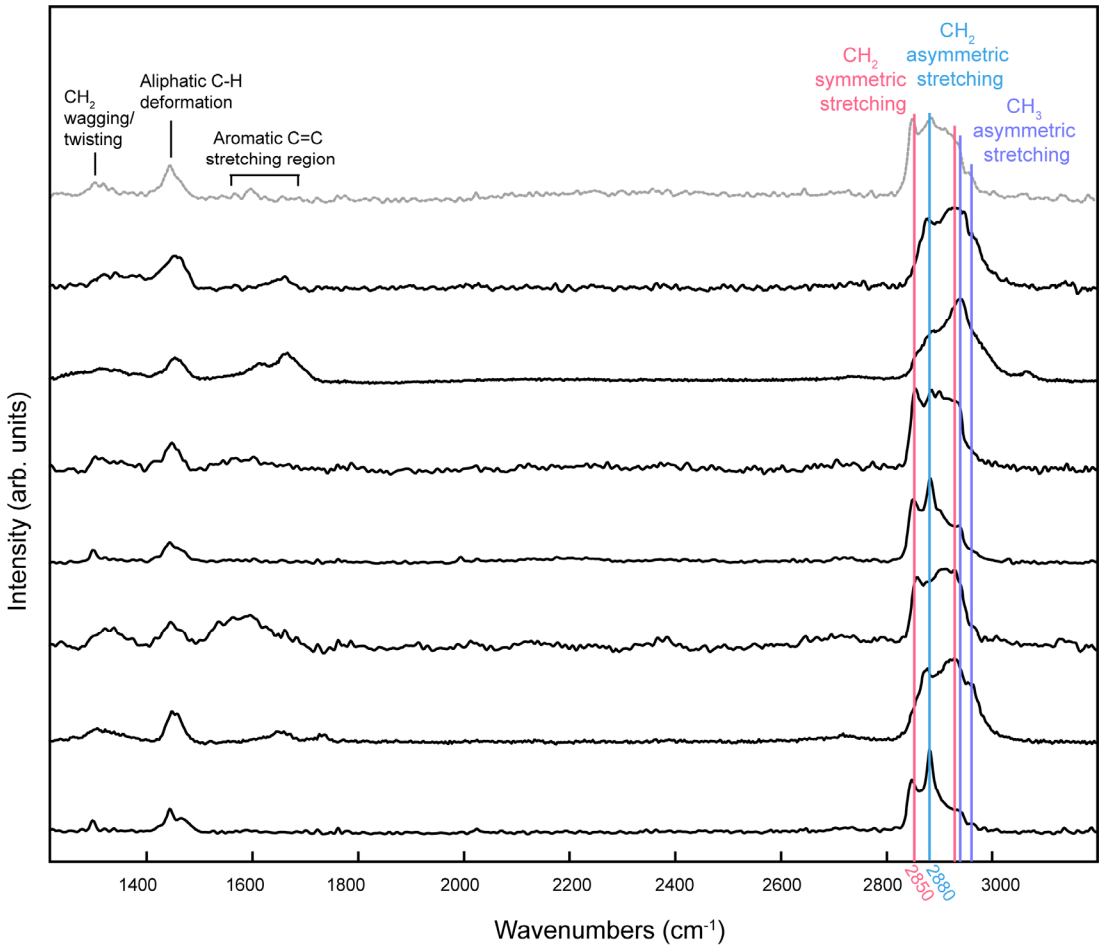

214

215 **Figure DR6.** Raman spectra of various micron-sized CCM within the investigated serpentinite
216 samples. These slightly different spectra corroborate the presence of aliphatic ± aromatic
217 compounds. The grey spectrum is equivalent to Fig. 3A shown in the main text.

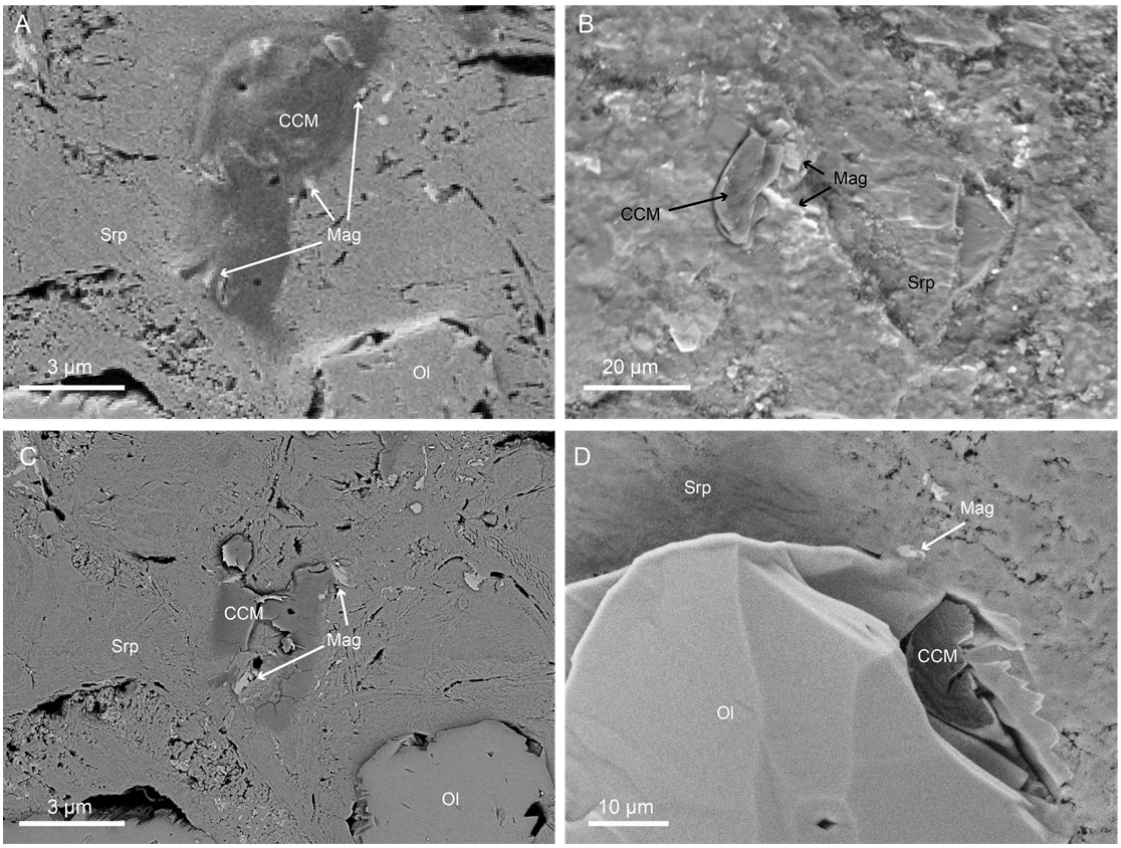

Figure DR7. Backscattered electron (BSE) images showing the distribution of carbonaceous matter within serpentinites. (**A**) CCM associated with magnetite (Mag) after step I. (**B**) The presence of organic patch and magnetite in a freshly broken serpentinite sample. (**C**) Residual CCM associated with magnetite after step II (images in A and C are from the same location). (**D**) Organic patch filling void between serpentinite (Srp) and olivine (Ol) after step III.

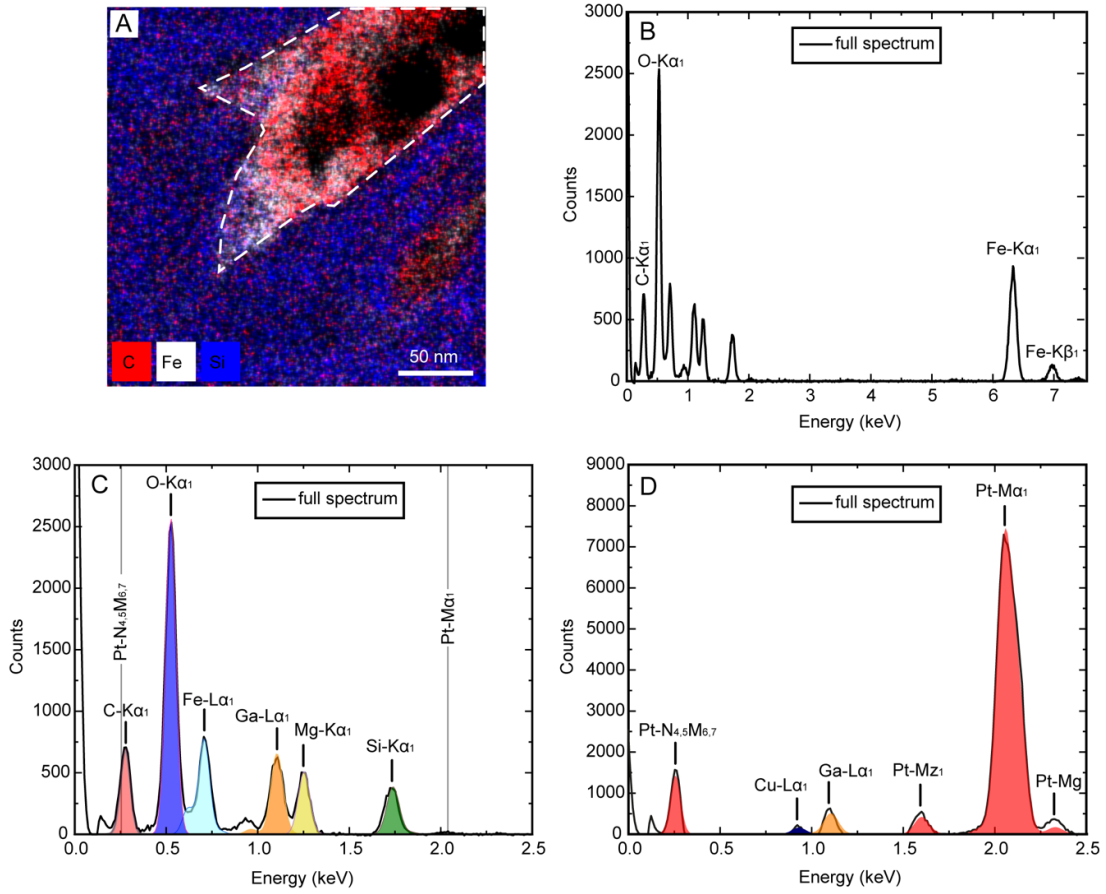

Figure DR8. Energy-dispersive X-ray (EDX) mapping within a (scanning) transmission electron microscope of the serpentine nanopore. (**A**) Equivalent EDX map as shown in Fig. 2F of the main article, where Si, Fe, and C denote serpentine, Fe-oxide and organic matter, respectively. (**B**) Full EDX spectrum of the area denoted by the dashed boarder in (A). (**C**) Magnified view of the spectrum shown in B at an energy range between 0 to 2.5 keV. Colored areas denoted fitted and deconvoluted spectra as executed in the Bruker ESPRIT 1.9 software package. We did not detect any Pt in the sample and the area of interest as highlighted by the lack of the Pt Mα1 line (position denoted by the through-going, grey line). For comparison, (**D**) shows the EDX signal from the Pt layer covering the FIB-SEM foil. This shows that the Pt metal organic precursor gas is completed decomposed during the deposition phase. Moreover, the C-Kα_1 peak originating for the organic matter in C is clearly distinguishable, and can be

237 deconvoluted, from any potential contribution of the $PtN_{4,5}M_{6,7}$ line (grey through-going line).

238 A quantitative analysis of the EDX data can be found in Table DR4.

239

Table DR4. Quantification of EDX-STEM data shown in Figure DR8.

	Sample (area shown in Fig. DR8A)		Pt layer of FIB-SEM foil	
	wt.%	2σ	wt.%	2σ
C	26.3	1.8	0	0
O	39.5	2.5		
Si	5.2	0.1		
Pt	0.0	0.0	94.5	19.0
Mg	6.2	0.5		
Fe	17.5	1.2		
Ga	5.4	0.5	5.5	0.6
Total	100.0		100.0	
C/Fe	1.5			

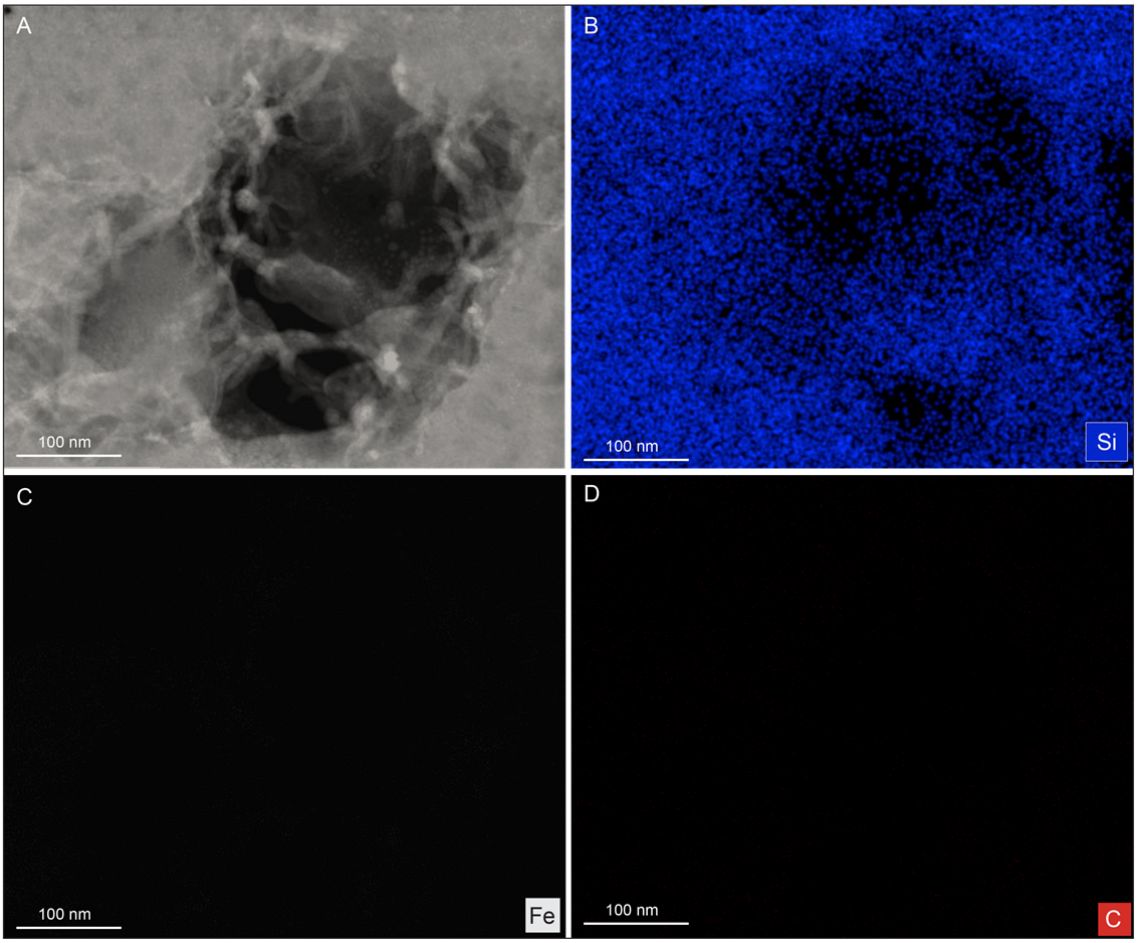

240

Figure DR9. TEM image showing neither identifiable carbonaceous matter nor Fe-oxide grains are present around the nanopore of mesh serpentine. (A) HAADF-STEM image of the nanopore. **(B, C, D)** are equivalent EDX maps in (A). Si, Fe, and C denote serpentine, Fe-oxide and carbonaceous matter, respectively.